Technical University of Denmark

DTU

Permanently reconfigured metamaterials due to terahertz induced mass transfer of gold

Strikwerda, Andrew; Zalkovskij, Maksim; Iwaszczuk, Krzysztof; Lorenzen, Dennis Lund; Jepsen, Peter Uhd

Link back to DTU Orbit

DTU Library
Technical Information Center of Denmark

Permanently reconfigured metamaterials due to terahertz induced mass transfer of gold

Andrew C. Strikwerda,[1,2] Maksim Zalkovskij,[1] Krzysztof Iwaszczuk,[1] Dennis Lund Lorenzen,[1] and Peter Uhd Jepsen[1,3]

[1]DTU Fotonik – Department of Photonics Engineering, Technical University of Denmark, DK-2800 Kgs. Lyngby, Denmark
[2]astr@fotonik.dtu.dk
[3]puje@fotonik.dtu.dk

Abstract: We present a new technique for permanent metamaterial reconfiguration via optically induced mass transfer of gold. This mass transfer, which can be explained by field-emission induced electromigration, causes a geometric change in the metamaterial sample. Since a metamaterial's electromagnetic response is dictated by its geometry, this structural change massively alters the metamaterial's behavior. We show this by optically forming a conducting pathway between two closely spaced dipole antennas, thereby changing the resonance frequency by a factor of two. After discussing the physics of the process, we conclude by presenting an optical fuse that can be used as a sacrificial element to protect sensitive components, demonstrating the applicability of optically induced mass transfer for device design.

References and links

1. H. Tao, C. Bingham, A. C. Strikwerda, D. V. Pilon, D. Shrekenhamer, N. Landy, K. Fan, X. Zhang, W. Padilla, and R. D. Averitt, "Highly flexible wide angle of incidence terahertz metamaterial absorber: Design, fabrication, and characterization," Phys. Rev. B **78**(24), 241103 (2008).
2. B. Reinhard, K. M. Schmitt, V. Wollrab, J. Neu, R. Beigang, and M. Rahm, "Metamaterial near-field sensor for deep-subwavelength thickness measurements and sensitive refractometry in the terahertz frequency range," Appl. Phys. Lett. **100**(22), 221101 (2012).
3. A. C. Strikwerda, R. D. Averitt, K. Fan, X. Zhang, G. D. Metcalfe, and M. Wraback, "Electromagnetic composite-based reflecting terahertz waveplates," Int. J. High Speed Electron. Syst. **20**(03), 583–588 (2011).
4. A. C. Strikwerda, K. Fan, H. Tao, D. V. Pilon, X. Zhang, and R. D. Averitt, "Comparison of birefringent electric split-ring resonator and meanderline structures as quarter-wave plates at terahertz frequencies," Opt. Express **17**(1), 136–149 (2009).
5. H. R. Seren, G. R. Keiser, L. Cao, J. Zhang, A. C. Strikwerda, K. Fan, G. D. Metcalfe, M. Wraback, X. Zhang, and R. D. Averitt, "Optically Modulated Multiband Terahertz Perfect Absorber," Adv. Opt. Mater. **2**(12), 1221–1226 (2014).
6. H.-T. Chen, J. F. O'Hara, A. K. Azad, A. J. Taylor, R. D. Averitt, D. B. Shrekenhamer, and W. J. Padilla, "Experimental demonstration of frequency-agile terahertz metamaterials," Nat. Photonics **2**(5), 295–298 (2008).
7. D. Shrekenhamer, S. Rout, A. C. Strikwerda, C. Bingham, R. D. Averitt, S. Sonkusale, and W. J. Padilla, "High speed terahertz modulation from metamaterials with embedded high electron mobility transistors," Opt. Express **19**(10), 9968–9975 (2011).
8. H.-T. Chen, W. J. Padilla, J. M. O. Zide, A. C. Gossard, A. J. Taylor, and R. D. Averitt, "Active terahertz metamaterial devices," Nature **444**(7119), 597–600 (2006).
9. T. Driscoll, S. Palit, M. M. Qazilbash, M. Brehm, F. Keilmann, B.-G. Chae, S.-J. Yun, H.-T. Kim, S. Y. Cho, N. M. Jokerst, D. R. Smith, and D. N. Basov, "Dynamic tuning of an infrared hybrid-metamaterial resonance using vanadium dioxide," Appl. Phys. Lett. **93**(2), 024101 (2008).
10. H. Tao, A. C. Strikwerda, K. Fan, W. J. Padilla, X. Zhang, and R. D. Averitt, "MEMS based structurally tunable metamaterials at terahertz frequencies," J. Infr. Millim. THz Waves **32**(5), 580–595 (2011).
11. L. Liu, W. Chen, D. A. Powell, W. J. Padilla, F. Karouta, H. T. Hattori, D. N. Neshev, and I. V. Shadrivov, "Post-processing approach for tuning multi-layered metamaterials," Appl. Phys. Lett. **105**(15), 151102 (2014).
12. M. Rahm, J.-S. Li, and W. J. Padilla, "THz Wave Modulators: A Brief Review on Different Modulation Techniques," J. Infr. Millim. THz Waves **34**(1), 1–27 (2013).
13. P. G. Slade and E. D. Taylor, "Electrical breakdown in atmospheric air between closely spaced (0.2 μm-40 μm) electrical contacts," IEEE Trans. Compon. Packag. Tech. **25**(3), 390–396 (2002).

14. M. Vincent, S. W. Rowe, C. Poulain, D. Mariolle, L. Chiesi, F. Houzé, and J. Delamare, "Field emission and material transfer in microswitches electrical contacts," Appl. Phys. Lett. **97**(26), 263503 (2010).
15. A. Semnani, A. Venkattraman, A. A. Alexeenko, and D. Peroulis, "Frequency response of atmospheric pressure gas breakdown in micro/nanogaps," Appl. Phys. Lett. **103**(6), 063102 (2013).
16. H. Hirori, A. Doi, F. Blanchard, and K. Tanaka, "Single-cycle terahertz pulses with amplitudes exceeding 1 MV/cm generated by optical rectification in LiNbO3," Appl. Phys. Lett. **98**(9), 091106 (2011).
17. A. Tarekegne, K. Iwaszczuk, M. Zalkovskij, A. C. Strikwerda, and P. U. Jepsen, "Impact ionization in high resistivity silicon induced by an intense terahertz field enhanced by an antenna array," New J. Phys. **17**(4), 043002 (2015).
18. N. C. J. van der Valk, T. Wenckebach, and P. C. M. Planken, "Full mathematical description of electro-optic detection in optically isotropic crystals," J. Opt. Soc. Am. B **21**(3), 622 (2004).
19. M. C. Hoffmann, J. Hebling, H. Y. Hwang, K.-L. Yeh, and K. A. Nelson, "Impact ionization in InSb probed by terahertz pump-terahertz probe spectroscopy," Phys. Rev. B **79**(16), 161201 (2009).
20. K. Fan, H. Y. Hwang, M. Liu, A. C. Strikwerda, A. Sternbach, J. Zhang, X. Zhao, X. Zhang, K. A. Nelson, and R. D. Averitt, "Nonlinear terahertz metamaterials via field-enhanced carrier dynamics in GaAs," Phys. Rev. Lett. **110**(21), 217404 (2013).
21. H. Hirori, K. Shinokita, M. Shirai, S. Tani, Y. Kadoya, and K. Tanaka, "Extraordinary carrier multiplication gated by a picosecond electric field pulse," Nat. Commun. **2**, 594 (2011).
22. C. A. Werley, K. Fan, A. C. Strikwerda, S. M. Teo, X. Zhang, R. D. Averitt, and K. A. Nelson, "Time-resolved imaging of near-fields in THz antennas and direct quantitative measurement of field enhancements," Opt. Express **20**(8), 8551–8567 (2012).
23. Handbook of Chemistry and Physics, 95th Edition," http://www.hbcpnetbase.com/.
24. TOPSIL, http://www.topsil.com/en/silicon-products/silicon-wafer-products/hires™.aspx.
25. P. S. Ho and T. Kwok, "Electromigration in metals," Rep. Prog. Phys. **52**(3), 301–348 (1989).
26. H. Park, A. K. L. Lim, A. P. Alivisatos, J. Park, and P. L. McEuen, "Fabrication of metallic electrodes with nanometer separation by electromigration," Appl. Phys. Lett. **75**(2), 301 (1999).
27. G. A. Mesyats, "A Cyclical Explosive Model of the Cathode Spot," IEEE Trans. Electr. Insul. **EI-20**(4), 729–734 (1985).
28. E. Hourdakis, B. J. Simonds, and N. M. Zimmerman, "Submicron gap capacitor for measurement of breakdown voltage in air," Rev. Sci. Instrum. **77**(3), 034702 (2006).
29. R. G. Forbes and J. H. B. Deane, "Reformulation of the standard theory of Fowler–Nordheim tunnelling and cold field electron emission," Proc. R. Soc. A Math. Phys. Eng. Sci. **463**, 2907–2927 (2007).
30. R. Tirumala and D. B. Go, "An analytical formulation for the modified Paschen's curve," Appl. Phys. Lett. **97**(15), 151502 (2010).
31. A. Peschot, N. Bonifaci, O. Lesaint, C. Valadares, and C. Poulain, "Deviations from the Paschen's law at short gap distances from 100 nm to 10 μm in air and nitrogen," Appl. Phys. Lett. **105**(12), 123109 (2014).
32. P. Rumbach and D. B. Go, "Fundamental properties of field emission-driven direct current microdischarges," J. Appl. Phys. **112**(10), 103302 (2012).
33. T. W. Dakin, "Breakdown of gases in uniform fields. Paschen curves for nitrogen, air and sulfur hexafluoride," Electra **32**, 61–82 (1974).
34. K. Iwaszczuk, M. Zalkovskij, A. C. Strikwerda, and P. U. Jepsen, "Nitrogen plasma formation through terahertz-induced ultrafast electron field emission," Optica **2**(2), 116–123 (2015).
35. L. Verlet, "Computer "Experiments" on Classical Fluids. I. Thermodynamical Properties of Lennard-Jones Molecules," Phys. Rev. **159**(1), 98–103 (1967).
36. Y. Itikawa, "Cross Sections for Electron Collisions with Nitrogen Molecules," J. Phys. Chem. Ref. Data **35**(1), 31 (2006).
37. R. F. Egerton, R. McLeod, F. Wang, and M. Malac, "Basic questions related to electron-induced sputtering in the TEM," Ultramicroscopy **110**(8), 991–997 (2010).
38. K. Takano, F. Miyamaru, K. Akiyama, H. Miyazaki, M. W. Takeda, Y. Abe, Y. Tokuda, H. Ito, and M. Hangyo, "Crossover from capacitive to inductive electromagnetic responses in near self-complementary metallic checkerboard patterns," Opt. Express **22**(20), 24787–24795 (2014).
39. K. Kempa, "Percolation effects in the checkerboard Babinet series of metamaterial structures," Phys. Status Solidi Rapid Res. Lett. **4**(8-9), 218–220 (2010).
40. Y. Nakata, Y. Urade, T. Nakanishi, and M. Kitano, "Plane-wave scattering by self-complementary metasurfaces in terms of electromagnetic duality and Babinet's principle," Phys. Rev. B **88**(20), 205138 (2013).
41. M. Liu, H. Y. Hwang, H. Tao, A. C. Strikwerda, K. Fan, G. R. Keiser, A. J. Sternbach, K. G. West, S. Kittiwatanakul, J. Lu, S. A. Wolf, F. G. Omenetto, X. Zhang, K. A. Nelson, and R. D. Averitt, "Terahertz-field-induced insulator-to-metal transition in vanadium dioxide metamaterial," Nature **487**(7407), 345–348 (2012).

1. Introduction

The need to customize electromagnetic responses has driven the field of metamaterials and led to significant advances in terahertz (THz) technology such as perfect absorbers [1], dielectric sensors [2], and polarization control [3,4]. These results have been further advanced using light [5,6], voltage [7,8], temperature [9], and structural change [10,11] for dynamic control [12] of the response. These impressive results have been possible because

metamaterials take their electromagnetic response mainly from their geometry rather than their chemistry, allowing remarkable freedom in design ingenuity.

Here we introduce a new technique for geometric modification of the metamaterial itself. This reconfiguration is achieved through mass transfer during exposure to intense THz radiation and is permanent, providing a form of writable memory that can be used in device design. The mass transfer is caused by field emission induced electromigration [13,14] and may have a substantial impact on high frequency electronics in the THz region, similar to electromigration at lower frequencies and, by further studying the physical process, could contribute to the understanding of microplasma generation and gas breakdown in AC fields [15]. Additionally, the ability to electrically connect two objects could potentially lead to a form of non-contact welding.

We begin by forming a conducting pathway between two isolated antennas, demonstrating the mass transfer phenomenon and then show how the sample's altered electromagnetic response can be modeled in simulation. Next, we discuss the underlying physical process involved in this phenomenon. We then present a practical THz device, which we call an optical fuse, that can be used as a sacrificial element to protect sensitive components from intense free space radiation, similar to its electrical circuit namesake.

2. Results

2.1 Observation of mass transfer

In Fig. 1 we show a scanning electron microscopy (SEM) image that is characteristic of the induced mass transfer due to intense THz radiation. The sample itself is an array of gold antennas fabricated on a high resistivity silicon (HR-Si) substrate using standard UV photolithography and e-beam gold deposition with a layer thickness of 200 nm. The unit cell of the array is a pair of antennas aligned end to end with a small gap between them as shown in Fig. 1. The extra material in Fig. 1(b) is gold - confirmed by energy-dispersive X-ray spectroscopy (EDX) - that has been displaced from the antenna tips.
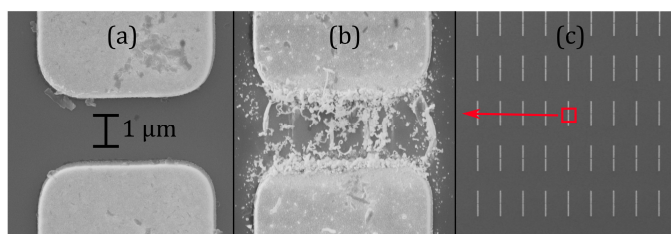

Fig. 1. SEM images of an antenna gap region before (a) and after (b) exposure to the intense THz radiation. The excess material in (b) is gold, as confirmed by EDX. (c) A larger image that shows the antenna array, as well as a red square identifying the gap between the antenna pair.

2.2 Experiment

The samples were measured using THz time domain spectroscopy (THz-TDS) powered by the output of a commercial regenerative amplifier generating 800 nm optical pulses of 5.5 mJ and 100 fs at a 1 kHz repetition rate. Most of the optical power was used to generate the THz transients in a $LiNbO_3$ crystal using a tilted pulse front configuration, similar to that described elsewhere [16,17]. The THz pulse was then directed through a pair of wire grid polarizers manually set to achieve a peak THz field of 200 kV/cm and a full width at half maximum (FWHM) of 300 μm at the sample spot. After the sample, two off axis paraboloid mirrors were used to image the pulse onto a GaP crystal where it was detected using electro-optic sampling [18]. An optical chopper, set at the first subharmonic of the laser, was placed in the generating beam line so that THz transients were incident on the samples at 500 Hz. All measurements were conducted in a dry nitrogen atmosphere and at the polarization of the electric field was parallel to the antennas at all times.

The measurements were performed using a THz electric field attenuated to 8 kV/cm. Between measurements, the samples were exposed to the full 200 kV/cm for approximately five minutes, and in all cases the THz radiation was incident upon the structured side of the sample rather than through the substrate [17]. This change in field strength was accomplished using nine HR-Si wafers as beam attenuators (200 kV/cm $\times 0.7^9 \approx 8$ kV/cm) which were inserted and removed from the beam path using an automated translation stage. This high field exposure / low field measurement technique is necessary to separate the permanently induced change due to mass transfer from any transient changes induced by high field effects in the substrate, such as impact ionization and intervalley scattering [17,19–21]. A simple schematic of this arrangement and the THz pulse used are shown in Fig. 2. As can be seen in Fig. 2(b), the spectral maximum of the pulse was optimized to match the resonance frequency of the samples [16].
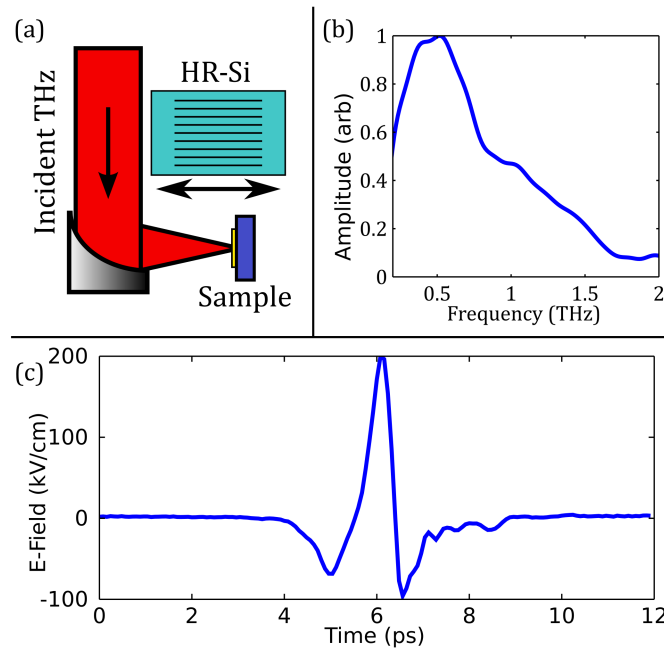

Fig. 2. (a) A subset of the THz-TDS setup. The HR-Si wafers that are inserted/removed from the beam line to enable high field exposure and low field THz-TDS measurement of the same location on a given sample.(b) The spectral content in the THz pulse. (c) The THz pulse in the time domain.

We measured samples with gaps of 2.5, 5, 7.5, and 10 μm, where the gap size refers to the spacing between the antennas as shown in Fig. 1 and 3(b). For all samples, each individual antenna has a length of 80.9 μm, width of 5 μm, and thickness of 200 nm and the unit cell size is 141 μm by 282 μm. The HR-Si wafer is 525 μm thick. While the 10 μm gap sample showed no detectable change, the other samples all experienced a significant modification of their broadband transmission as a function of exposure time to the THz radiation. As an example, we present the permanently induced change in transmission for a 2.5 μm sample in Fig. 3(d) and 3(f).
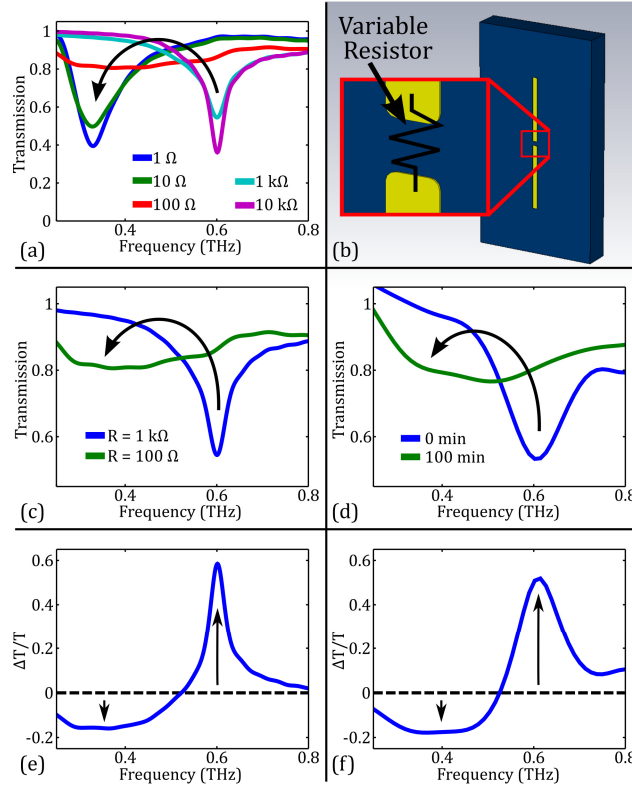
Fig. 3. A combination of simulated (left column) and experimental (right column) results. (a) Several transmission spectra for varying resistances. (b) The unit cell with the variable resistor clearly identified in the antenna gap. (c) and (d) Broadband comparison for the 5 μm gap sample. (e) and (f) The *ΔT/T* for the scans in (c) and (d), respectively.

The *ΔT/T* in Fig. 3(f) is due to a permanent buildup of gold in the gap region, as seen in Fig. 1. As we demonstrate in the simulation section, this gold accumulation can be modeled as a decrease in resistivity between the two antennas that essentially shorts out the antenna gap. The spectral change can then be easily explained using the standard equation for the resonance frequency of an antenna

$$frequency = \frac{c}{2nL} \tag{1}$$

where *L* is the antenna length, *n* is the effective refractive index of the dielectric environment, and *c* is the speed of light. As the gap region shorts out, the two antennas connect electrically and start to behave as a single antenna with twice the original antenna length. By effectively doubling the antenna length, the resonance frequency decreases by a factor of two.

2.3 Simulation

To gain a better understanding of this behavior, we performed full wave computer simulations using CST Microwave Studio using a conductivity of gold of 4.561×10^7 S/m and HR-Si index of refraction of index of 3.417. The simulated unit cell, shown in Fig. 3(b), is as described earlier with the addition of a lumped element resistor added across the gap. By changing the resistance (*R*) we can mimic varying amounts of gold buildup. In the absence of any induced change (i.e. Figure 1(a)), the resistance is high (*R* > 1 kΩ) and the antennas resonate near their design frequency of 0.6 THz. As the resistance decreases, mimicking the migration of gold between the antennas, the original resonance disappears and is eventually

replaced by a new resonance at 0.33 THz in accordance with the prediction of Eq. (1). This simulated change in transmission versus *R* is shown in Fig. 3(a). To demonstrate the validity of this model, Fig. 3(c) and 3(e) show simulated spectra for comparison with the experimental data shown in Fig. 3(d) and 3(f). The simulated curves were chosen "by eye" and we do not, as yet, have a method for calculating the appropriate *R* to use in simulation for a given structure, field strength, and exposure time.

The computer simulations also allow us to estimate the electric field values at the antenna tips and these values are summarized in Table 1. Note that the field enhancement values are sampled in the time domain, where we have used the experimentally measured THz pulse in Fig. 2(c) as the simulated THz excitation. The values were sampled 10 nm from the antenna. For all samples the enhancement at the opposite tips (i.e. the "outer" tip) was 36 times.

Table 1. A summary of the electric field enhancements.

Gap Size (μm)	Field enhancement	Total field (MV/cm)
2.5	62	12
5	49	9.7
7.5	44	8.8
10	42	8.3
Outer tip	36	7.3

Total field is simply the field enhancement times a 200 kV/cm incident field. The "Outer tip" refers to the antenna tip away from the gap region, which was constant across all samples.

2.4 Transmission change vs time/resistance

As another comparison with experiment, the *ΔT/T* for simulations with varying resistances is shown in Fig. 4(a). In this figure, each horizontal line represents a simulation performed at a given *R*. The *ΔT/T* is then calculated using the *R* = 10 kΩ transmission as the initial state, so that the bottommost line is 0 by definition and every other line is the percentage change. For comparison, Fig. 4(b) shows the experimental *ΔT/T* as a function of THz exposure time for the 7.5 μm sample. In this plot, each transmission scan is normalized to the pre-exposure transmission in the same way as the simulated data set so again, the bottom line is 0 by definition. In this way, we can see that a decreasing *R* in simulation correlates with increasing THz exposure time in experiment. Phrased in a more physically intuitive manner, the THz radiation is causing gold to migrate into the gap region and this can be modeled as a decrease in resistance. More exposure time causes more migration and lower resistance.
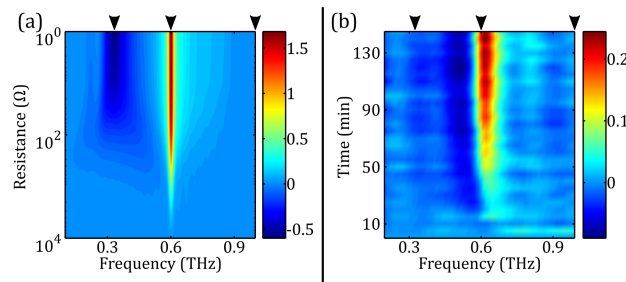

Fig. 4. (a) The simulated *ΔT/T* as a function of resistance. (b) The experimental *ΔT/T* as a function of high field exposure time. The arrows above the plots correspond to the single frequency trend lines shown in Fig. 5.

In Fig. 5 we further compare the experimental and simulated *ΔT/T* by looking at single frequency lines at 0.33, 0.6, and 1.0 THz. As in Fig. 4, there is strong qualitative agreement between the experimental data and the simulated predictions. We can also see that the samples with smaller gaps, and therefore stronger electric field enhancements [22], experience faster and larger changes in transmission. As the gap size increases, the *ΔT/T* decreases until the 10 μm sample which shows no detectable change despite high field exposure of over 16 hours

(not shown). This is addressed further in section 4 when discussing the physical process. This figure also demonstrates why the 7.5 µm sample data set was chosen for Fig. 4; the transmission for samples with smaller gaps changed too rapidly to be monitored in detail with the time resolution available in our experimental configuration. The slow changing 7.5 µm sample is actually more interesting in that context.
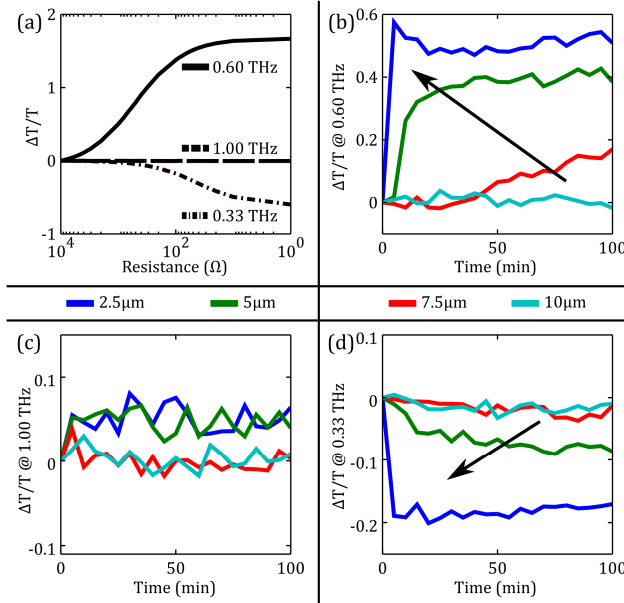

Fig. 5. Single frequency trend lines for simulation (a) and experiment at (b) 0.33, (d) 0.6 and (c) 1.0 THz. These lines correspond to vertical slices of the *ΔT/T* plots, and triangles are located at the top of Fig. 4(a) and 4(b) as a visual aid. The simulation is for the 5 µm gap antenna, but is characteristic of all gap sizes. (b)-(d) show the experimental changes in the samples of various gap size. The arrows in each plot demonstrate how samples with smaller gap sizes experience larger transmission changes in shorter times.

3. Discussion

3.1 Differences in simulation vs experiment

When drawing the correlation between simulation and experiment, it is worth identifying two major limitations. The first, related to the significant difference in broadening, is that simulation models an infinite array of identical unit cells, while in experiment we have a Gaussian beam profile. Due to the field dependent nature of the effect, this means that the unit cells in the beam center experience relatively large amounts of change, while the unit cells near the beam periphery may experience none at all. The experimental THz-TDS scan will effectively perform a spatial average of the antennas in the beam spot, resulting in a substantial amount of broadening in the transmission spectra when compared to simulation.

The second major difference is that the magnitude of the experimental *ΔT/T* is significantly less than that of simulation. While this can be partially attributed to several factors, perhaps the most significant is that the mass transfer in these samples appears to exhibit a threshold-like behavior. We attribute this to a correlation between the field enhancement and the gap resistance. The strong field enhancement is due to large oscillating charge concentrations across the gap as the antennas resonate. However, as more and more metal accumulates in the gap region, the resistance decreases and the charge accumulation will conduct from one antenna to the other. This conducting pathway decreases the charge concentration, which decreases the field enhancement, which eventually decreases the rate of mass transfer.

3.2 Estimated resistivity

We can also use the simulated resistance value to obtain an order of magnitude value for the resistivity (ρ) achieved by the mass transfer. If we take the $R = 100$ Ω effective value from Fig. 3(c), we can then use

$$R = \frac{\rho L \eta}{A} \qquad\qquad (2)$$

where *A* is the antenna cross section (5 μm × 200 nm) and *L* is the 2.5 μm gap. We have modified the traditional equation by adding in a dimensionless filling factor *η*, which we set to 0.1, to account for the fact that not all of the gap volume is filled with conductor, ie. Figure 1(b). These approximations yield an effective resisitivity of 4×10^{-6} Ωm which can be compared to the resistivity of Au (2.05×10^{-8} Ωm) [23] and HR-Si (>10 kΩm) [24]. While this is almost 200 times larger than bulk Au, it is six orders of magnitude lower than the HR-Si wafer without mass transfer. Again, we stress that this is an effective value, and we anticipate the resistivity in the beam center to be lower than this number. If a low enough resistivity can be achieved, this could enable a method of non-contact optical welding.

4. Physical process

The general process of electric fields inducing mass transfer in continuous metal wires, called electromigration, has existed for over fifty years. A similar phenomena has also been observed between electrical contacts at lower frequencies [13] but, to the best of our knowledge, this is the first observation using free space radiation at THz frequencies. We motivate our discussion by briefly discussing the history of electromigration.

4.1 Electromigration

Traditional electromigration is, literally, electrically driven migration, and is most commonly associated with direct current in conductors. This process is the result of competition between the direct force of the electric field on the atomic lattice and the "electron wind" force due to momentum transfer from conduction electrons to the lattice via scattering events. This, and other contributing factors such as temperature, stress, and strain gradients, cause the atomic lattice to deform along grain boundaries, surfaces, and through bulk material [25]. Sufficient migration causes voids and hillocks and has historically been a major cause of electronic device failure, although it has also been used beneficially, for example in the creation of nanometer sized gaps for single-electron transistors [26].

4.2 Mass transfer across an air gap

The same basic principle, strong currents generate mass transfer, has been observed across closely spaced electrical contacts [13]. For large gap separations, this has been explained by microexplosions on the cathode [27] while a recent report on nanogaps indicates impact heating on the anode via electron bombardment [14]. In either case, the similarity to traditional electromigration is clear; the strong current is simply traversing a gap instead of occurring in a continuous conductor.

We believe that the mass transfer we observe is due to material evaporation via electron impact heating. We will return to this point after introducing the physics of Paschen's law and our electron transport model in the next two sections.

4.3 Paschen's law

Paschen's law describes the breakdown voltage at gap separations greater 10 μm [28] and is originally based on an induced avalanche current between the contacts. Once an electron is liberated from the cathode, it will be accelerated by the electric field and collide with, and ionize, an atmospheric molecule. After the ionization process, there are two electrons accelerated by the electric field, starting the avalanche process and eventually resulting in current between the two contacts.

There has long been an experimental deviation from Pashcen's law for small gap separations (< 10 μm), where the experimentally measured breakdown voltage was much lower than anticipated by theory. In these cases, Paschen's law overestimates the required breakdown voltage due to a decrease in the number of avalanche processes that can occur over short distances. This deviation has recently been accounted for by including electron field emission via the Fowler-Nordheim equation [29]. This contribution more than compensates for the reduced number of ionization events, substantially reducing the breakdown voltage [30–32].

To compare our antenna samples with previously observed breakdown voltages, we integrated the simulated electric field across the gap for all our samples and compared the voltages to the experimental values for N_2 breakdown [33]. Once the aforementioned field emission is considered, the only anomalous sample is the antenna with the 10 μm gap. Simulation yields a voltage of over 800 V across the gap region, much higher than the breakdown voltage of 260 V in literature [33], and suggestive of strong electron transport. Therefore the question is not why is there mass transfer in our samples, but rather, why is there no mass transfer in the 10 μm sample?

4.4 Electron transport

To help answer this question, we highlight the two major differences between our experiment and previous measurements. First, the previous values were measured with homogeneous fields instead of the significantly inhomogeneous fields between our antennas. However, the massive field enhancement near our antenna tips should *increase* the electron field emission relative to the homogeneous case, resulting in an even larger current. For these antenna samples, field emission can be detected using a Photomultiplier Tube (PMT) [34] and we have experimentally observed field emission for the 10 μm sample and insolated antennas [34] without any mass transfer and conclude that this is not the source of the disagreement.

We believe that the second difference, the high frequency of our electric field as opposed to the previous DC measurements, is the cause for the discrepancy [15]. To model the high frequency response, we used the time dependent spatial profile of the electric field in the gap from computer simulation. We then solved

$$\ddot{\vec{r}} = \frac{q\vec{E}(\vec{r},t)}{m_e} \qquad (3)$$

using a velocity Verlet method [35] where r is position; q and m_e are the charge and mass of the electron; and $\vec{E}(\vec{r},t)$ is the electric field in space and time. The initial conditions were for an electron starting at an antenna tip with zero velocity and the calculation was conducted until the electron reached the opposite antenna tip. The initial time, t_0, was varied to minimize the transit time and interactions between the electron and the dry N_2 atmosphere were neglected.

The minimum transfer times were 0.25, 0.49, 0.75, and 1.08 ps for the 2.5, 5, 7.5, and 10 μm samples, respectively, and the results are summarized in Fig. 6. The increasing transition time is due to the increasing gap size, the decreasing field enhancement, and the oscillatory nature of the electric field since the FWHM of the pulse in Fig. 2(c) is only 0.45 ps. For example, Fig. 6(b) shows that the electron considered in the 10 μm gap calculation barely crosses the antenna gap. Its energy at impact is only 47 eV and the direction of the electric field has flipped during transit, resulting in a strong braking force via the antenna enhancement factor.

Further complicating this trip, we reiterate that the calculation neglects N_2 interactions. We present the total cross section of N_2 in Fig. 6(c), reproduced from [36]. Figure 6(d) shows the collision time, which is ~0.1 ps for most of the journey. Note that this collision time is from the total cross section, so it includes scattering, momentum transfer, rotation, vibrational and electronic excitations, as well as ionization and radiation emission.
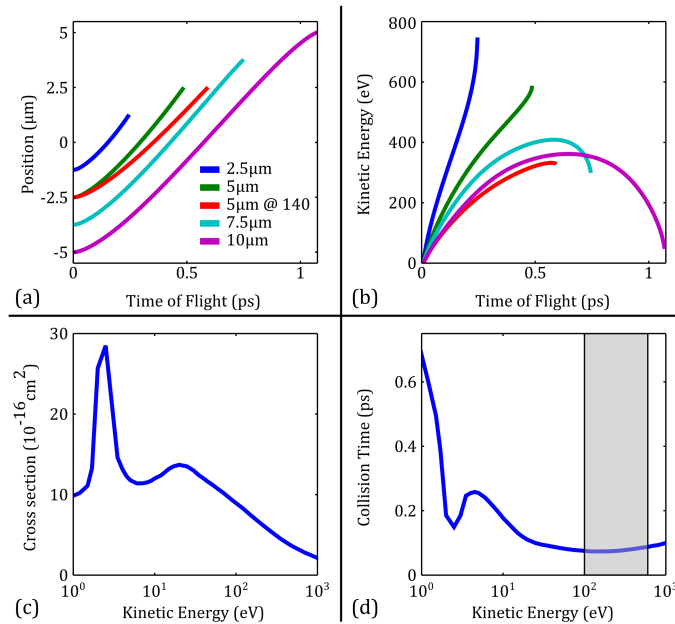
Fig. 6. Position (a) and kinetic energy (b) of an electron vs time for the calculations from Eq. (3). The incident electric field is 200 kV/cm for all curves, except the one labeled 5 μm @ 140 which is 140 kV/cm. The total cross section (c) for free electrons in N_2 and the expected collision time (d) are plotted vs the electron kinetic energy. Since the electrons have 100s of eV of energy during most of their journey, the region of 100 eV – 600 eV is highlighted in (d). The data in (c) is directly from [36] and (d) is calculated from (c).

4.5 Impact heating

We now return to our claim that the mass transport is due to impact heating [14] via electron bombardment, as opposed to the microexplosions theory.

The microexplosions theory says that "microexplosions arise on passing the field electron emission current" [27]. The current, which is due to field emission, only depends on the local electric field and the work function [29]. This means that if the microexplosions theory is correct, stronger local electric fields experience greater amounts of mass transfer.

To test this theory, we measured a 5 μm sample with a maximum field of 140 kV/cm and still observed a clear permanent change in transmission (data not shown). When combined with the simulated field enhancements in Table 1, this means that the in gap field was 140 kV/cm × 49 = 6.8 MV/cm. This is lower than both the in gap field of the 10 μm sample (8.3 MV/cm) or the field at the outer tip of the antennas (7.3 MV/cm), neither of which showed any indication of electromigration in either transmission measurements or SEM images. This is in direct contradiction with the microexplosions theory.

Instead, we conduct our electron transport model on a 5 μm sample with an incident field of 140 kV/cm. As seen in Fig. 6, the electron easily traverses the gap with substantially more kinetic energy than the 10 μm sample despite having a lower local electric field strength, consistent with our claim of impact heating.

We also have preliminary results confirming that the mass transport occurs more rapidly when measured in vacuum. This is also consistent with the impact heating model, due to the reduced scattering events, and suggests that pressure can be used to modify the rate of transmission change. However, these measurements are still ongoing.

4.6 Physical process summary

Before continuing, we summarize the physical process and identify why the antennas with smaller gaps show more rapid transmission changes.

1. The material transfer is likely due to impact heating from electron bombardment. This requires numerous electrons with substantial kinetic energy.

2. Field emission is strongly nonlinear with electric field.

3. Smaller gaps have greater electric field enhancements, resulting in many more free electrons via field emission.

4. Once liberated from the antenna, electrons in smaller gap samples are accelerated more rapidly due to the greater field enhancement.

5. Electrons in smaller gap samples have a shorter distance to travel.

6. Since their trip is shorter, electrons in smaller gap samples have fewer atmospheric interactions.

7. Electrons for sufficiently large gaps experience a braking force due to the oscillating electric field, massively reducing their kinetic energy.

4.7 Other potential contributions

Here we briefly discuss, and reject, the contributions of electron sputtering and Joule heating to the mass transfer process.

4.7.1 Electron sputtering

We have already confirmed that the antennas are being bombarded by energetic electrons from the opposite antenna. This process is virtually identical to electron sputtering. However, a simple calculation suggests that the sputtering threshold for gold is over 400 keV [37], roughly three orders of magnitude larger than the electron energies in Fig. 6. We conclude that this is not a sputtering process.

4.7.2 Joule heating

Here we consider the linear thermal problem, where we are specifically referring to the ohmic losses induced in the antenna by the THz field. This does not include impact heating via nonlinear field emission. We do not believe that Joule heating is a contributing factor for two reasons.

The first is that the absorption spectra from computer simulation, which is solely due to ohmic losses, are relatively constant with gap size. Therefore, all samples will experience a similar temperature increase under irradiation. The second is that the thermal effects should be largest in the region of highest current density, which is in the center of the antenna and not in the gap.

To examine the possibility of thermal build up over time, we calculated the time integral of the resistive losses in the antenna from simulation, yielding the total absorbed energy per antenna per pulse. Using this number, the physical dimensions of the antennas, and the thermal properties of gold, we calculate an average temperature increase of 0.33 K in the antenna after one THz pulse. We then used this temperature increase as an initial condition in a thermal simulation that considered conduction into the substrate and convection into the air. For the thermal simulations, which were conducted in COMSOL Multiphysics, we used a thermal conductivity of gold σ_{Au} = 314 W/K/m; density ρ_{Au} = 19320 kg/m^3; heat capacity at constant pressure $C_{p,Au}$ = 130 J/kg/K and correspondingly, for HR-Si we used σ_{Si} = 130 W/K/m; ρ_{Si} = 2329 kg/m^3; $C_{p,Au}$ = 700 J/kg/K. The antenna temperature returns to within 0.01 K of ambient temperature in less than 0.2 μs. As mentioned in the experimental section, the 1 kHz laser is chopped at its first sub harmonic prior to the LiNbO$_3$ crystal, providing 2 ms for thermal relaxation between successive THz pulses. We conclude that ohmic losses are not a contributing factor.

5. Optical fuse

Since we have seen that optically induced mass transfer can permanently damage a sample, we have designed an optical fuse to prevent critical samples from unintentional damage. The fuse operates on the same mass transfer process we have just discussed.

5.1 Operation

The fuse, shown in Fig. 7(c), is an array of conducting squares arranged like a checkerboard. The beauty of this structure lies in its very high sensitivity to small geometric changes at the point between adjacent squares [38]. The near-self-complementary structure is a geometric singularity and is a topological analog of the percolation threshold [39]. We refer the interested reader elsewhere [39,40] for a more thorough theoretical discussion.

The operation of the fuse is remarkably simple. When the metallic squares are unconnected, the structure is a bandstop filter at a frequency determined by its period and the refractive index of the substrate. When the squares are physically connected, the bandstop filter becomes a bandpass filter at the same frequency [38]. However, we are only interested in the low frequency behavior below the bandpass/bandstop frequency. When the metallic squares are unconnected the low frequency transmission is near 1, since it is much lower than the bandstop frequency. When the squares are connected the low frequency transmission is near 0, since it is much lower than the bandpass frequency.

Therefore, the fuse is simply an array of unconnected metallic squares and the period is chosen so that the THz pulse is transmitted with low attenuation. In the presence of a strong THz field, the gold atoms will migrate and form a conducting path between adjacent squares, shifting the checkerboard from a bandstop to a bandpass filter, effectively "blowing" the fuse. A simulation demonstrating this behavior is shown in Fig. 7(a).
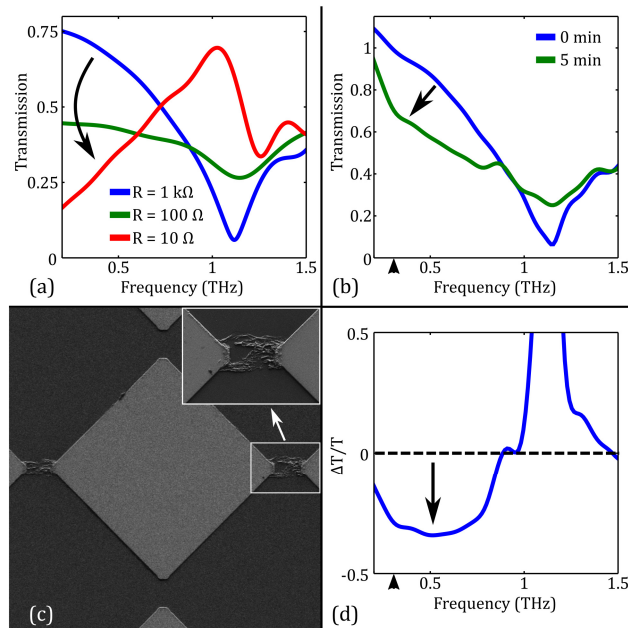

Fig. 7. (a) Simulated and (b) experimental transmission spectrum showing the effect of physically connecting the 75 μm checkerboard squares. The small arrow on the x-axes of both (b) and (d) is the low frequency cutoff discussed in the text. (c) SEM images after THz exposure. (d) ΔT/T for the two scans in (b).

5.2 Experimental results

Fabricated samples, with periods of 25, 50, 75, and 100 μm and a 1.5 μm gap between the squares, were measured in a manner similar to that described earlier except that the wire grid polarizers were removed for a maximum field of 234 kV/cm. An SEM image of an exposed optical fuse is shown in Fig. 7(c). Note that the sample is clearly polarization sensitive, as the gold accumulation is only between squares that are horizontally adjacent, matching the polarization of the incident field. However, there are other near-self-complementary structures that could be used to exhibit different behavior.

The experimental data in Fig. 7, which is for the 75 μm period fuse, clearly demonstrates a broadband decrease in transmission of over 30%, which is over 50% in power, for a 400 GHz bandwidth. When compared with the simulated results in Fig. 7(a), there is a major discrepancy at low frequencies which we attribute to the beam spot issue discussed in section 3.1. Again, the simulation results consider an infinite array of identical unit cells while the THz beam only induces mass transfer near the center of the beam. To argue this, we assume that frequencies can only be blocked where the continuous conducting path of metallic squares is greater than a wavelength. The FWHM of the beam spot size is approximately 300 μm and we assume that every square inside of the FWHM is connected and none of the ones outside are. Then, factoring in the substrate index, this yields a cutoff frequency of 0.3 THz which is in reasonable agreement with the experimental results in Fig. 7. The cutoff frequency is indicated by a small arrow on the x-axis of Fig. 7(b).

The results for periods of 25, 50, and 100 μm, while not shown, demonstrate similar behavior to Fig. 7 in that they disagree with simulation at low frequencies and have a high frequency limit determined by their period. For example, the 100 μm and 50 μm samples have transmission decreases of over 25% for 280 GHz and 774 GHz, respectively. The 25 μm sample did not show the same magnitude of extinction, but demonstrated a decrease of approximately 20% for over 1.1 THz. The 50 μm sample demonstrated the largest transmission extinction, over 40%, which we believe is due to the best bandwidth matching between that sample and our experimental pulse.

Due to the rapid increase in high power THz systems, nonlinear THz behavior, and THz technology in general, we anticipate unintentional THz induced mass transfer to be a significant problem if left unaccounted for. Similar to a traditional fuse, this checkerboard can be used as a sacrificial element to protect sensitive optical components. For example, Liu, et al. experienced irreversible THz induced damage to a sample of metamaterials on a VO_2 thin film [41]. That is, of course, a contrived example where high field THz radiation was intentionally combined with the field enhancement of a metamaterial to induce a nonlinear effect. However, it clearly demonstrates that if the damage tolerances are well understood, a simple sample of gold on commercially available HR-Si could be sacrificed instead of a specially grown thin film. As we saw with the antenna structures in Fig. 5, the gap between adjacent squares can be adjusted to change the "blow" time of the optical fuse. More exotic uses that take advantage of either the transition from bandpass to bandstop or the pressure dependent mass transfer rates are not hard to imagine.

6. Conclusion

In conclusion, we have demonstrated a new technique for metamaterial device design using mass transfer induced by intense THz radiation. This technique causes a permanent geometric change in the sample and can be used to form conducting pathways between two otherwise insulated metallic structures. Not only does this potentially provide a pathway towards non-contact welding, it also identifies a likely hurdle towards high frequency THz electronics and could provide insight into microplasma generation and air breakdown. As a specific design example, we presented a proof of principle demonstration of an optical fuse at THz frequencies, which can be used to protect sensitive THz components from unwanted damage. We hope that this work will contribute to further advances in our physical understanding of

mass transfer, as well as providing to another useful design technique in the metamaterial toolbox.

Acknowledgments